Journal of Materials Research and Technology 37 (2025) 5237–5250

Contents lists available at ScienceDirect

Journal of Materials Research and Technology

journal homepage: www.elsevier.com/locate/jmrt

Hot deformation behavior and dynamic recrystallization of AD730 Ni-based superalloy in a wide range of temperatures and strain rates

Z. Mirzaie [a], G.R. Ebrahimi [b,*], H.R. Ezatpour [c,**]

[a] Department of Materials and Polymers Engineering, Faculty of Engineering, Hakim Sabzevari University, Sabzevar, Iran
[b] Department of Materials Science and Engineering, Faculty of Engineering, Ferdowsi University of Mashhad, Mashhad, Iran
[c] Department of Materials Engineering, Vali-e-Asr University of Rafsanjan, Rafsanjan, Iran

ARTICLE INFO

Keywords:
AD730 Ni-Based superalloy
Hot compression test
$\acute{\gamma}$ precipitates
DRX

ABSTRACT

In this study, the flow behavior, microstructural evaluation and dynamic recrystallization (DRX) mechanisms of a new AD730 Ni-based superalloy with initial coarse grain size were investigated by hot compression tests in a wide temperature range of 950–1200 °C and strain rates of 0.001 s^{-1}, 0.01 s^{-1}, 0.1 s^{-1} and 1 s^{-1}. According to the dissolution temperature of the $\acute{\gamma}$ precipitates in the studied alloy at 1079 °C, a significant difference was observed in the flow stress, activation energy and microstructure in the two temperature ranges of 950–1050 °C and 1100–1200 °C for all strain rates. In the temperature range of 950–1050 °C, higher stress level in flow curves and activation energy value (1284.9 kJ/mol) were obtained. Microstructural observations showed that the high-volume fraction of fine $\acute{\gamma}$ precipitates formed during heating up to deformation temperature and holding at 950–1050 °C prevented DRX development which resulted in the formation of cracks and a non-uniform deformation. In the temperature range of 1100–1200 °C, the dissolution of $\acute{\gamma}$ fine precipitates decreased the flow stress level and the activation energy to 468.94 kJ/mol as a result of development of DRX. DRX in coarse grain AD730 was occurred by strain induced boundary migration (SIBM) and particle stimulated nucleation (PSN) mechanisms which was enhanced by the twins.

1. Introduction

The increase of performance in gas turbines needs the development of new alloys which can serve at elevated temperatures. In the path of development of high application C & W Ni-based superalloys such as TMW4, IN718, Waspaloy, U720 and U720Li, Aubert & Duval French company introduced a new Ni-based superalloy as called "AD730″ for manufacturing of turbine disc in the jet motors [1–3]. However, TMW4, 718plus and U720i have limitations due to high content of Co in the chemical composition, restricted creep properties and high production cost, respectively, while AD730 presents an especial combination of the properties at elevated temperatures which has low production cost due to the existence of Fe (~4 wt%) and controlling the expensive elements content in its chemical compositions [3–7]. AD730 superalloy is a polycrystalline alloy with precipitation hardening ability by $\acute{\gamma}$ coherent phase with structure of L_{12} and composition of Ni_3(Al, Ti) which presents proper mechanical properties at 700 °C in comparison with the mentioned superalloys [1,8]. In development of AD730 superalloy, some researches have been down about aging [9,10], creep [11], corrosion behavior [6,12,13] and the effect of heat treatment on $\acute{\gamma}$ precipitates morphology and mechanical properties [4,8,14–17]. However, there are limited published reports about the hot compressive behavior of AD730 superalloy at elevated temperatures. So, the study on the dominant work softening mechanisms such as DRX during hot deformation with considering to the initial microstructure and the deformation parameters and achieving a fine grain microstructure can provide new findings in the direction of the development of high-performance Ni based superalloys.

Dynamic recovery (DRV) and DRX as main work softening mechanisms can occur during hot deformation of metal alloys. DRX as a well-known mechanism in the metals with low and medium stacking fault energy (SFE) such as Ni-based superalloys is accompanied with nucleation and growth of new grains. Therefore, the mechanical properties of the superalloys are dependent on DRX rate and final average grain size [18,19]. Flow behavior and work softening mechanisms in Ni-based superalloys are affected by deformation parameters such as

* Corresponding author.
** Corresponding author.
E-mail addresses: r.ebrahimi@um.ac.ir (G.R. Ebrahimi), h.ezatpour@vru.ac.ir (H.R. Ezatpour).

https://doi.org/10.1016/j.jmrt.2025.07.131
Received 21 May 2025; Received in revised form 7 July 2025; Accepted 14 July 2025
Available online 16 July 2025

Table 1
Chemical composition of AD730 Ni-based superalloy in wt. %.

Al	Ti	W	Nb	Mo	Cr	Co	Fe	C	B
2	2.7	2.8	0.98	3	14.5	9.8	4.8	0.0043	0.008

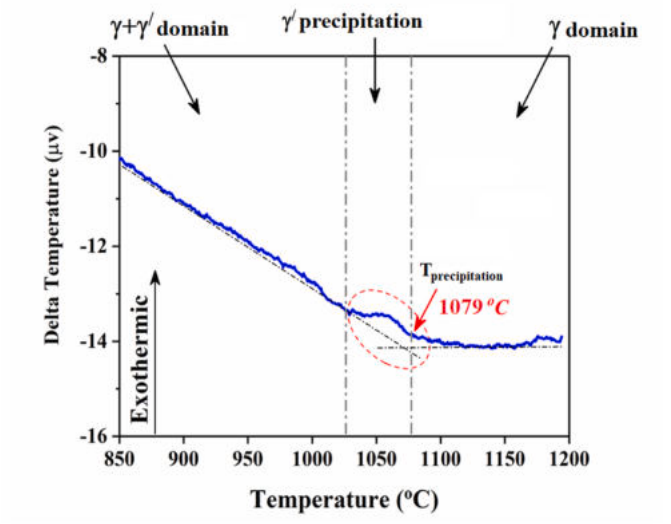

Fig. 1. DTA results during the cooling route of the cast-homogenized AD730.

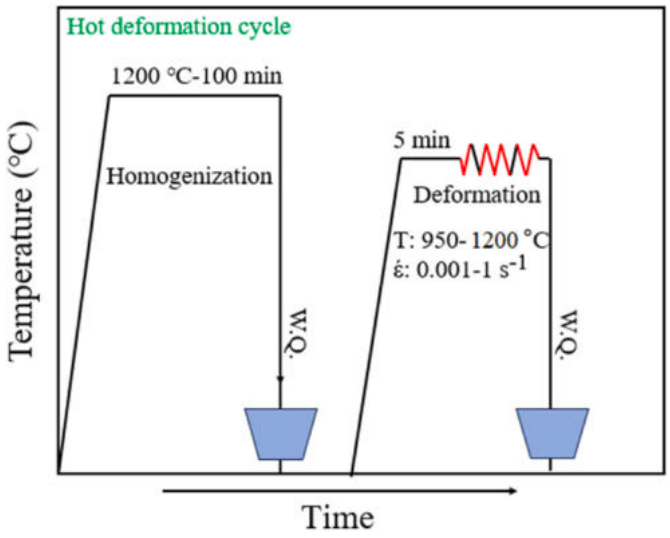

Fig. 2. Schematic representation of the thermomechanical treatment performed in the present study.

temperature (T), strain rate (ε̇), strain (ε) and initial microstructure characteristics such as initial grain size, precipitates and carbides. Wang et al. [20] studied microstructure changes of Inconel 718 by DRX. They reported that DRX rate increases with increasing the process temperature. Chen et al. and Lin et al. [21,22] indicated that the increase of process temperature or the decrease of strain rate raises the driving force of DRX in a nickel-based superalloy. Konkova et al. [14] expressed that the size of DRXed grains in AD730 decreases with increasing the strain rate. Liu et al. [23] observed nucleation and growth of DRXed grains from the grain boundaries in the temperature range higher than solution temperature in U720. They showed that easier DRX occurs in U720 with smaller initial grain size. Generally, in Ni-based superalloys with low SFE, discontinuous DRX (DDRX) which is accompanied with nucleation and growth of new grains has been introduced as the main mechanism of work softening [24,25]. Also, continuous DRX (CDRX) with gradual changes in sub grain boundaries has been observed in some conditions of the hot deformation, not as the main mechanism [26–28]. Song et al. [29] stated that the first nuclei during DRX forms by bulging of the parts of grain boundaries with SIBM mechanism which finally leads to formation of a necklace microstructure. Wang et al. [26] reported that after the start of DRX by bulging mechanism and formation of new grains in Inconel 740, twins can enhance the rate of nucleation and growth of DRXed grains. Zhong et al. [24] in the investigation of DRX mechanism in Incoloy 825 indicated that twins help to the enhancement of DRX by their transformation to high angle boundaries (HABs). Liu et al. [23] showed that DRX rate decreases considerably with the presence of precipitates during hot deformation of U720. So, the precipitate particles can affect the DRX mechanism during hot deformation process depending on their type, size and distribution [30,31]. Rollet et al. [31] showed that precipitates can play the role of an obstacle against DRX progression when their volume fraction to radius ratio is $> 0.2\ \mu m^{-1}$. It has been reported that in Co-based superalloys, fine precipitates prevent the formation of fine DRXed grains during hot deformation [32]. In contrast, coarse precipitates (>1 μm) can help to DRX by PSN mechanism [33]. Wang et al. [34] reported that the presence of coarse precipitates of Ni_3Nb (δ) can develop DRX during hot deformation.

AD730 superalloy as a precipitation hardened alloy with $\acute{\gamma}$ precipitates experiences DRX during hot deformation process at elevated temperatures. So, exploring the hot deformation behavior, the role of $\acute{\gamma}$ precipitates and carbides on the microstructure evolution and work softening mechanisms in a wide temperature range of 950–1200 °C and strain rates of 0.001–1 s^{-1} can be interesting for readers and industries. Therefore, flow curves analyzing, constitutive equation and microstructure characterizations are used to present a simple understanding of the hot deformation behavior of AD730 superalloy.

2. Experimental procedures

In this research, AD730 as a billet with dimensions of 6 * 5.6 * 28 cm^3 was casted by vacuum induction melting technique under a vacuum atmosphere of 10^{-3} bar. Chemical composition of as-cast AD730 is reported in Table 1.

For the hot deformation process, the cylindrical samples with diameter of 8 mm and height of 12 mm were machined from an as-cast billet. Then, all samples were homogenized at 1200 °C for 100 min according to the solution temperature of 1079 °C of $\acute{\gamma}$ phase (obtained from differential thermal analysis (DTA) as shown in Fig. 1),

Hot deformation process of AD730 was performed in the temperature range of 950–1200 °C and the strain rate range of 0.001–1 s^{-1} up to the strain of 0.8 by Zwich/Roell tensile testing machine equipped by an electrical furnace with temperature controller system with precision of ±5 °C. Before deformation, the samples were held at testing temperature for 5 min to remove the temperature slope. The schematic illustration of the hot deformation process is illustrated in Fig. 2. Also, for understanding of work softening mechanisms at elevated temperatures, some hot deformation tests were carried out at 1150 °C, 0.1 s^{-1} for strains of 0.2, 0.4 and 0.6.

Microstructures of hot deformed samples were characterized by the optical microscopy after etching by Marble solution (50 ml HCl + 50 ml H_2O + 10 g $CuSO_4$). EBSD measurements were carried out on a Hitachi SU-70 FEG-SEM operated at 20 kV and equipped with the Channel 5 software (Oxford Technology, English) and a step size of 0.25 μm.

To examine the precipitates morphology variations during hot deformation process, microstructures of samples were characterized by

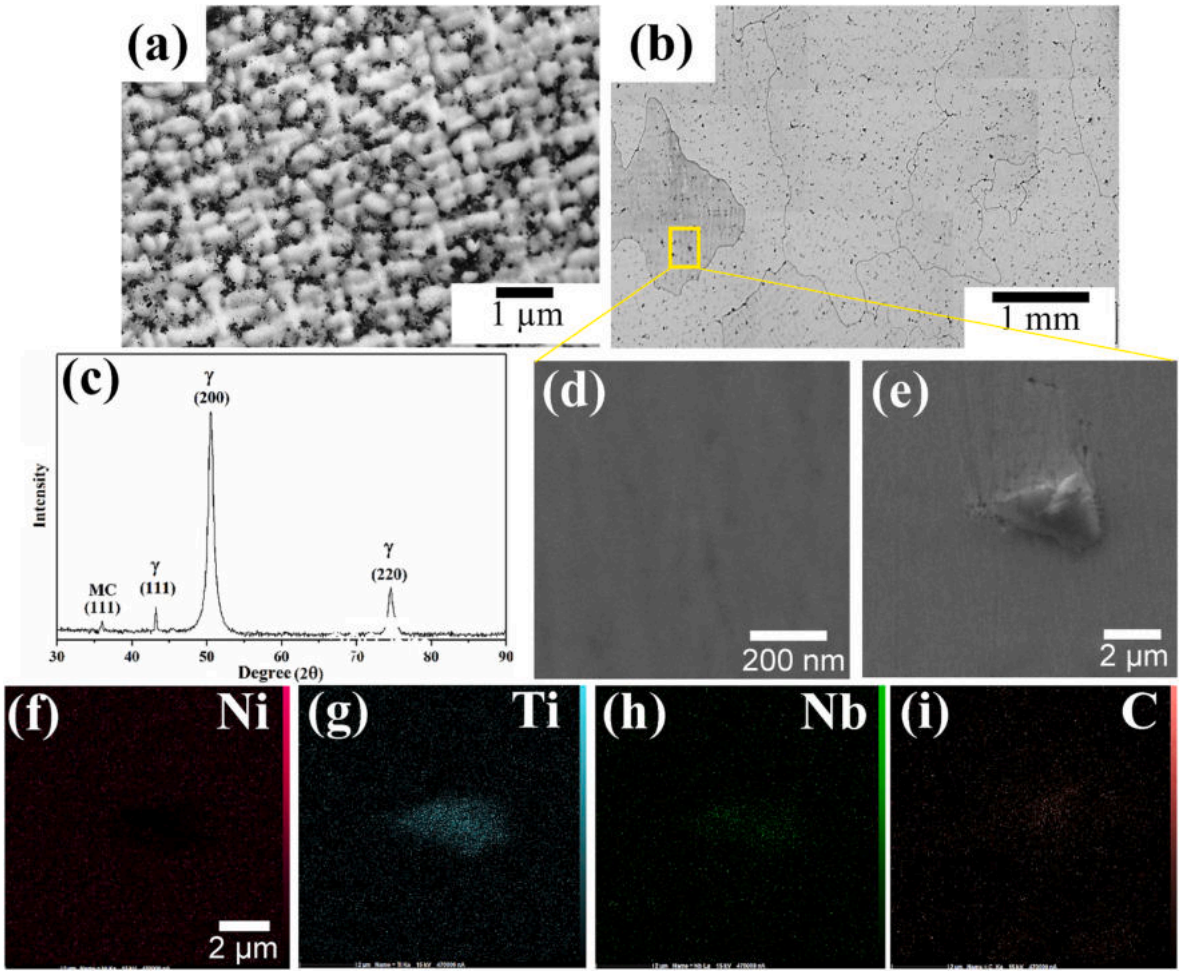

Fig. 3. (a, b) Optical micrographs of AD730 in conditions of (a) as-cast, (b) homogenized at 1200 °C for 100 min, (c) XRD analysis, (d, e) SEM images and (f–i) elemental maps of homogenized sample indicating the carbides type.

frequently scanning electron microscopy (FESEM; model: Mira3 TESCAN) before hot deformation (after heating and holding at deformation temperatures of 950 °C, 1000 °C and 1050 °C for 5 min) and after deformation in these temperatures at strain rate of 0.001 s^{-1}.

3. Results and discussion

3.1. Microstructures before hot deformation

Microstructures, XRD analysis and elemental maps of AD730 in as-cast condition and before and after solution heat treatment have been shown in Fig. 3. As is seen in Fig. 3(a), microstructure in as-cast condition is dendritic. After solution heat treatment at 1200 °C for 100 min (Fig. 3(b)), the dendritic structure in as-cast condition is eliminated and replaced with coarse grains of >1 mm. Some dark color particles with size of 3–4 μm (Fig. 3(e)) are observed which have a volume fraction of about 5 %. XRD analysis (Fig. 3(c)) and elemental maps (Fig. 3(f–i)) after solution treatment confirm that these particles are MC type carbide and rich of Ti, C and other elements such as Ni and Nb. Also, it should be mentioned that nanometric precipitates of $\acute{\gamma}$ are not detected in XRD pattern and high magnification FESEM image (Fig. 3(d)) which confirm all of them have been resolved after solution treatment.

3.2. Hot deformation behavior

3.2.1. The true stress-true strain curves

The true stress-true strain curves of AD370 after hot deformation in the temperature range of 950–1200 °C and strain rates of 0.001 s^{-1}, 0.01 s^{-1}, 0.1 s^{-1} and 1 s^{-1} up to strain of 0.8 after removing adiabatic and friction effects have been illustrated in Fig. 4. Results show that the stress level (peak stress, σ_p) decreases with increasing the temperature and decreasing the strain rate as shown in Fig. 5. The stress level at temperatures of 950 °C, 1000 °C and 1050 °C is more than temperatures of 1100 °C, 1150 °C and 1200 °C which can be attributed to microstructure evolutions. Also, the curves at low temperatures of 950 °C and 1000 °C and high strain rates of 0.1 s^{-1} and 1 s^{-1} show a final strain of <0.6 in comparison with other temperatures and strain rates because of flow instability such as grain boundary cracking, flow localization and fracture [35].

The flow curves at temperatures of 1100 °C, 1150 °C and 1200 °C show that the stress firstly increases to peak strain rapidly (step I: strain hardening) and then drops with increasing strain (step II: work softening) and finally reaches a steady state (step III). With consideration of the solution temperature of $\acute{\gamma}$ phase of AD730 at 1079 °C (as shown in Fig. 1), it seems that different mechanisms take part during hot deformation in up (1100–1200 °C) and down (950–1050 °C) temperature ranges of the solution temperature.

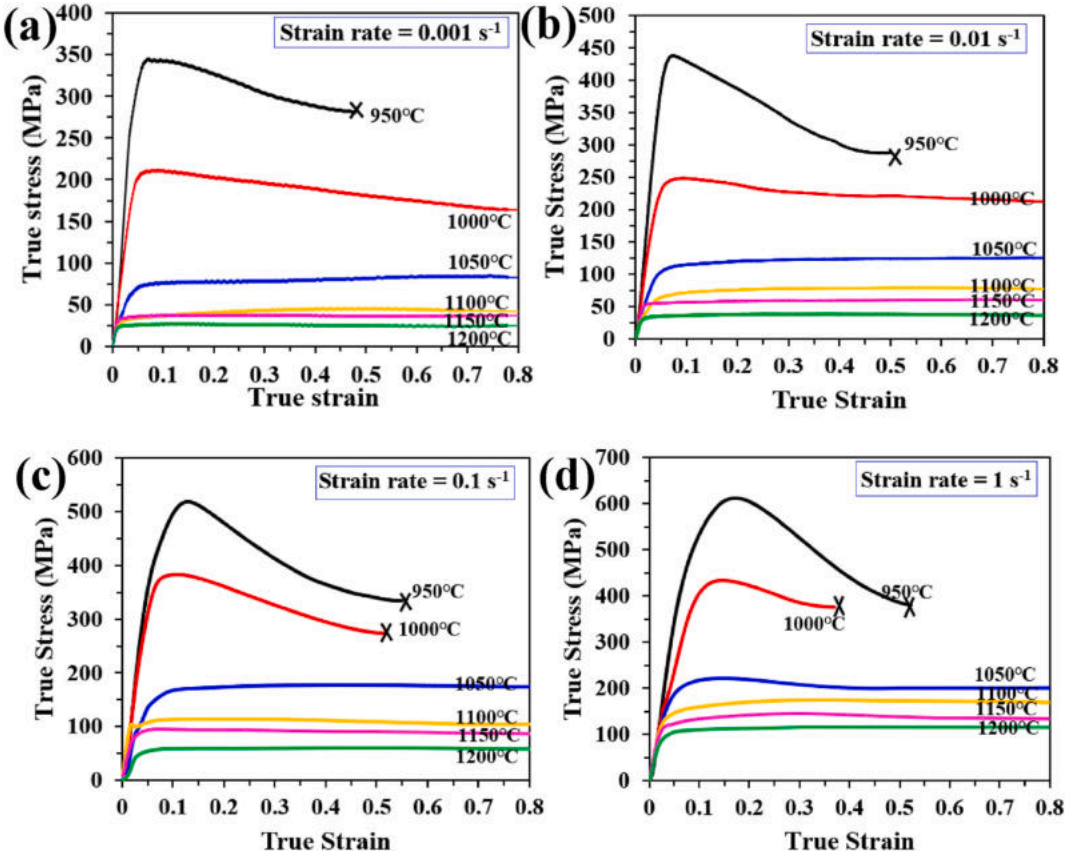

Fig. 4. The true stress-true strain curves of AD730 hot deformed in the temperature range of 950–1200 °C and strain rates of (a) 0.001 s^{-1}, (b) 0.01 s^{-1}, (c) 0.1 s^{-1} and (d) 1 s^{-1}.

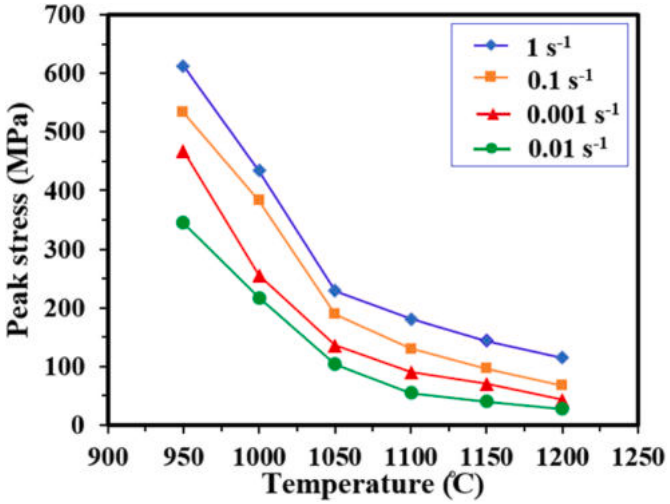

Fig. 5. The plot of peak stress vs. temperature at different strain rates.

To obtain activation energy of AD730 for illustrating a relationship among deformation parameters of stress, temperature and strain rate at different temperature ranges of 950–1050 °C and 1100–1200 °C, a sine hyperbolic function (Eq. (1)) is used in this study due to its application in a wide range of temperatures and strain rates [31,36]:

$$Z = \dot{\varepsilon}\exp\left(\frac{Q}{RT}\right) = A(\sinh(\alpha\sigma))^n \quad \text{(Eq. 1)}$$

where Z, Q, R and T are defined as Zener-Holoman parameter, activation energy, gas universal constant (=8.314 J/molK) and process temperature. A, n (stress exponent) and α are material constants.

α parameter is determined by following equation:

$$\alpha \approx \frac{\beta}{n'} \quad \text{(Eq. 2)}$$

where β and $\acute{n}$ can be obtained by the average slopes of the log $\dot{\varepsilon}$-log σ and log $\dot{\varepsilon}$-σ plots (Fig. 6(a and b)) defined by Eqs. (3) and (4):

$$n' = \left(\frac{\partial \log \dot{\varepsilon}}{\partial \log \sigma_p}\right)_T \quad \text{(Eq. 3)}$$

$$\beta = \left(\frac{\partial \log \dot{\varepsilon}}{\partial \sigma_p}\right)_T \quad \text{(Eq. 4)}$$

α values for AD730 are calculated as 0.0035 and 0.0126 for temperature ranges of 950–1050 °C and 1100–1200 °C, respectively.

By taking the natural logarithm of Eq. (1) and interpolating the empirical data obtained from stress–strain curves, Q can be determined by Eq. (5) and the average slopes of the log $\dot{\varepsilon}$-log sinh(ασ) and log sinh (ασ)-1/T plots as shown in Fig. 6(c and d):

$$Q = 2.3\left(\frac{\partial \log \dot{\varepsilon}}{\partial \log\left(\sinh(\alpha\sigma_p)\right)_\sigma}\right)_T \left(\partial\left(\frac{\log\left(\sinh(\alpha\sigma_p)\right)_\sigma}{\partial\left(\frac{1}{RT}\right)}\right)_{\dot{\varepsilon}}\right) \quad \text{(Eq. 5)}$$

So, activation energies values are determined as 1160.45 and 468.32 kJ/mol for two temperature ranges of 950–1050 °C and 1100–1200 °C, respectively which are in agreement with the values reported for different superalloys in the literature (Table 2).

Results show that there is a comparable difference between the flow

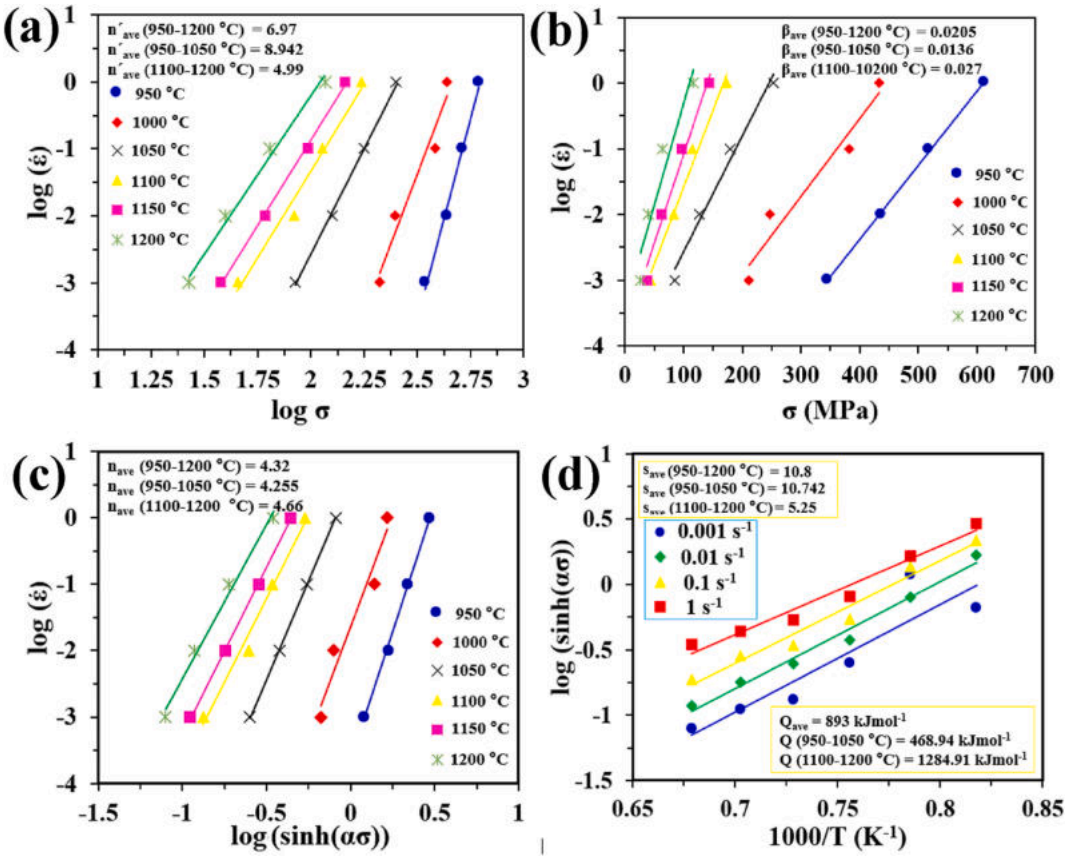

Fig. 6. Plots of (a) log $\dot{\varepsilon}$-log σ, (b) ln $\dot{\varepsilon}$-σ, (c) log $\acute{\varepsilon}$-log (sinh(ασ)) and (d) log (sinh(ασ))-1000/T for calculation of $\acute{n}$, β, n and Q in different strain rate and in the temperature ranges.

Table 2
Activation energies (kJ/mol) of different superalloys as compared to the present work.

Superalloy	Solution temperature of γ' (°C)	Q (kJ/mol)		Refs.
		single-phase region	two-phase region	
Waspaloy	1030	462	1400	[37]
In939	1080	400.5	930.1	[38]
Cobalt-based superalloy	1071	496.5	1182.5	[32]
U720Li	1140	417	687	[39]
NiCo based superalloy	1090	390	650	[40]
GH4742	1086	437.66	949.08	[41]
Present work	1079	468.32	1160.45	–

stresses and the activation energies for these two temperature ranges. At low temperatures or two phases region (γ + $\acute{\gamma}$ region) high flow stress and activation energy can be attributed to the presence of fine $\acute{\gamma}$ precipitates through the microstructure which prevent the movement of the dislocations and grain boundaries for the start of work softening mechanisms (pinning effect of precipitates) [37–39,42,43]. So, AD730 shows low formability in the temperature range of 950–1050 °C while the deformation needs to consume more energy. At elevated temperature range or single-phase region (γ region), low flow stress and activation energy is due to easy movement of dislocations and grain boundaries while enhance the work softening mechanisms such as DRX [32,44]. This region (1100–1200 °C) is corresponded with high formability of the alloy due to easier occurrence of work softening mechanisms.

3.3. Microstructures

3.3.1. Microstructures in the temperature range of 950–1050 °C

Microstructures of deformed samples at temperatures of 950 °C, 1000 °C, 1050 °C and strain rates of 0.001 s^{-1} to 1 s^{-1} have been shown in Fig. 7. Microstructures show elongated coarse grains with size of >1 mm. Also, the presence of grain boundary cracks, flow localization and adiabatic shear bands indicate non uniform deformation or the region with low formability. Similar observations have been also reported by Monajati et al. [45], Sajjadi et al. [46] and Sani et al. [32]. Although, microstructures especially at higher temperatures of 1000 °C and 1050 °C show very low fraction

of new fine DRXed grains into the grains and/or grain boundaries, these new grains almost are not observed considerably in the

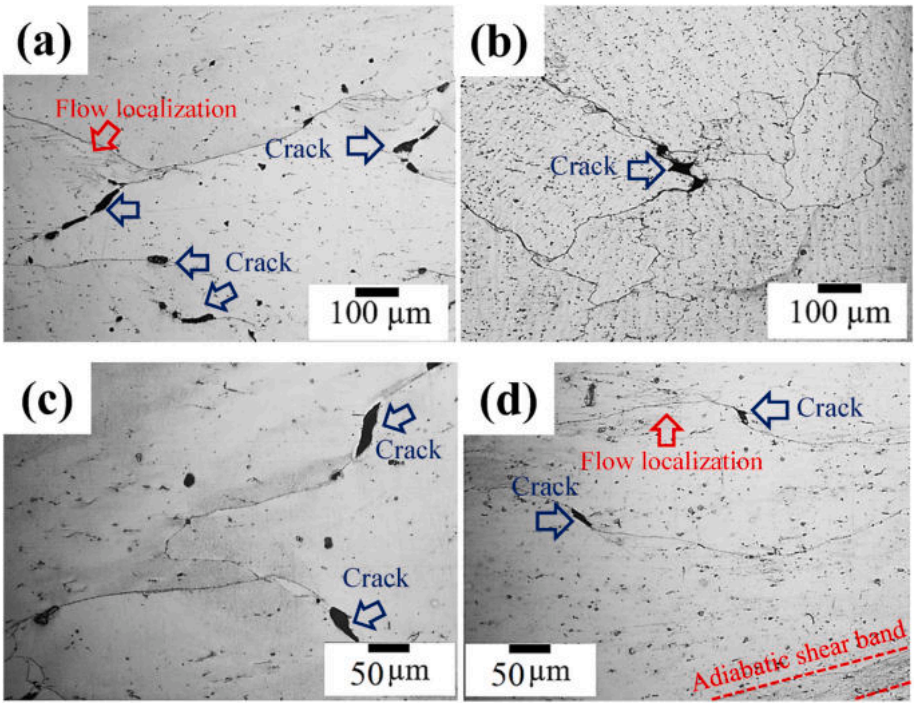

Fig. 7. Optical micrographs of deformed samples at (a) 950 °C-0.001 s^{-1}, (b) 950 °C-1 s^{-1}, (c) 1000 °C-0.001 s^{-1} and (d) 1050 °C-0.001 s^{-1}.

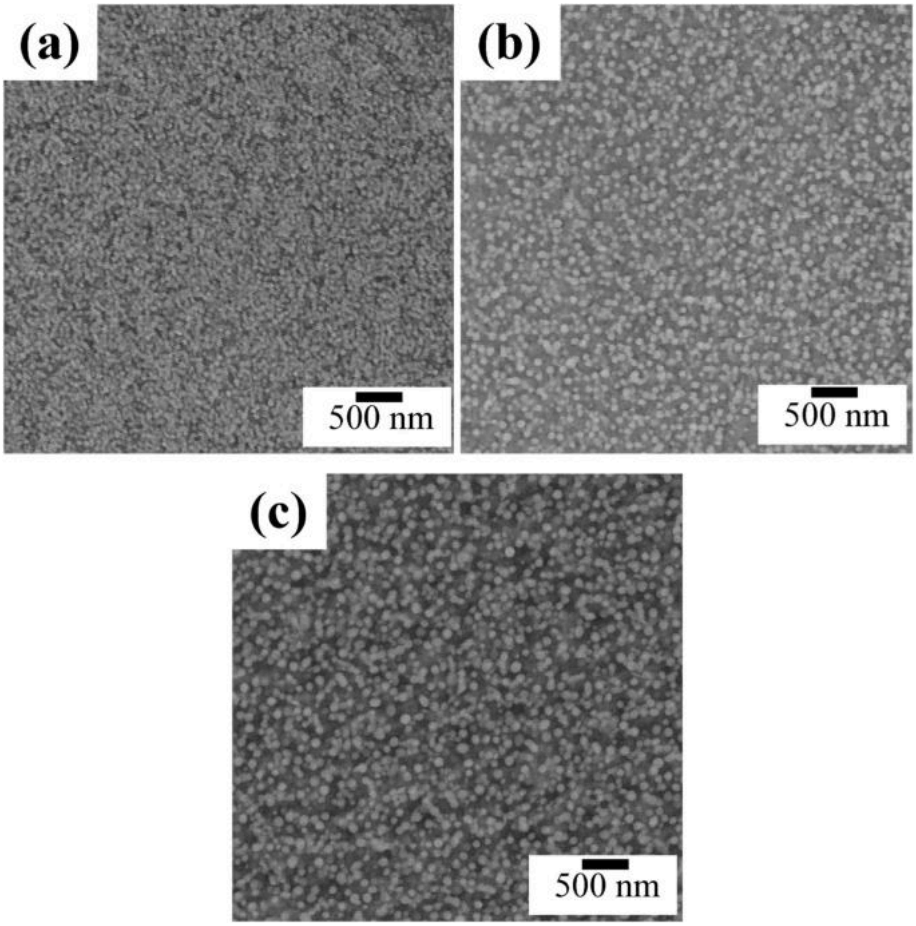

Fig. 8. Microstructures of samples after heating and holding at deformation temperature for 5 min, just before the hot compression tests at temperatures of showing morphology and distribution of the precipitates at (a) 950 °C, (b) 1000 °C and (c) 1050 °C.

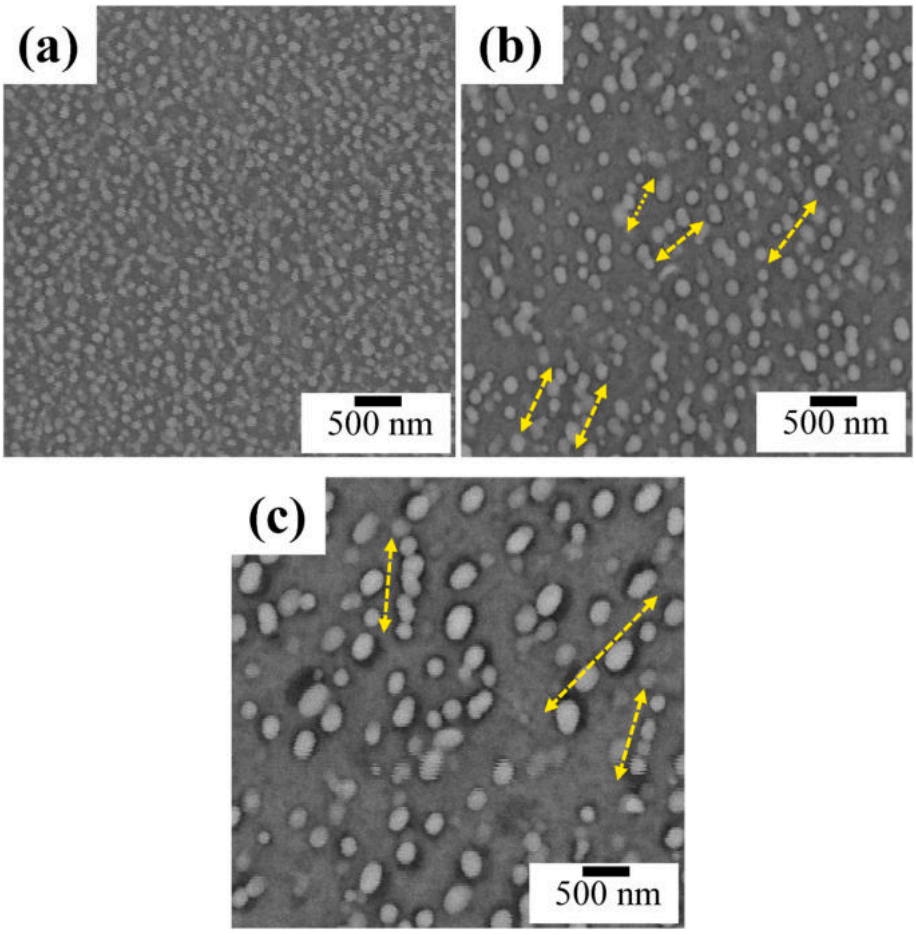

Fig. 9. Microstructures of samples showing morphology and distribution of the precipitates after hot deformation at strain rate of 0.001 s^{-1} and deformation temperatures of (a) 950 °C, (b) 1000 °C and (c) 1050 °C.

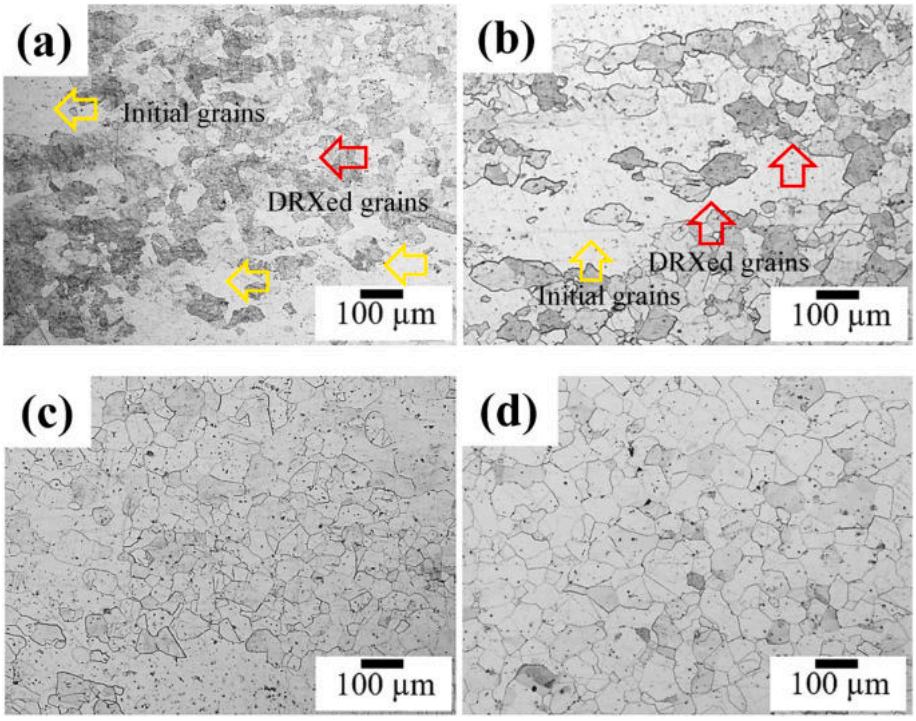

Fig. 10. Optical micrographs of deformed samples at (a) 1100 °C-0.01 s^{-1}, (b) 1150 °C-0.01 s^{-1}, (c) 1150 °C-0.1 s^{-1} and (d) 1200 °C-0.1 s^{-1}.

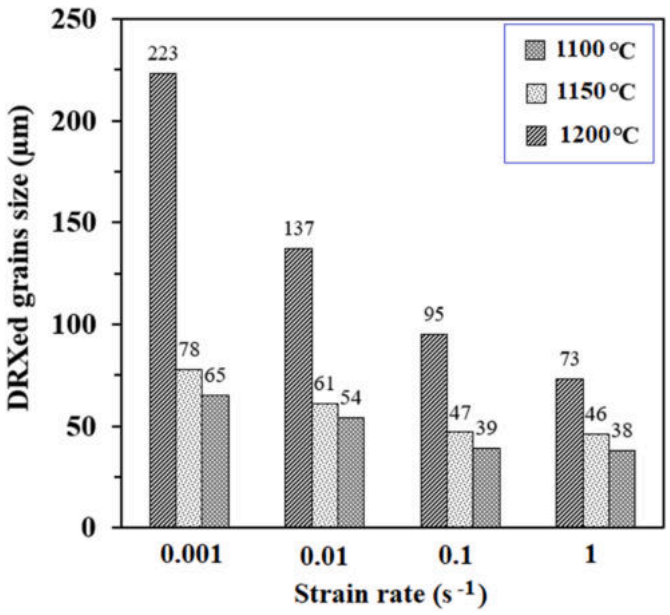

Fig. 11. The plots of the average size of DRXed grains versus (a) temperature and (b) strain rate.

Table 3
The values of σ_p, σ_s, ε_p and ε_s of AD730 at different deformation conditions.

Temperature (°C)	Strain rate (s^{-1})	σ_p (MPa)	σ_{ss} (MPa)	ε_p	ε_s
1100	0.001	35.83	42.99	0.08	0.3
	0.01	71	77.82	0.093	0.32
	0.1	113.72	106	0.193	0.48
	1	173.75	171	0.346	0.57
1150	0.001	35.23	37.2	0.046	0.28
	0.01	55.728	59.12	0.0501	0.3
	0.1	96.01	92.17	0.07	0.36
	1	144.6	134.9	0.295	0.59
1200	0.001	25.36	26.85	0.05	0.13
	0.01	35.1	38.2	0.05	0.15
	0.1	59	59.47	0.11	0.27
	1	97.74	96.18	0.24	0.48

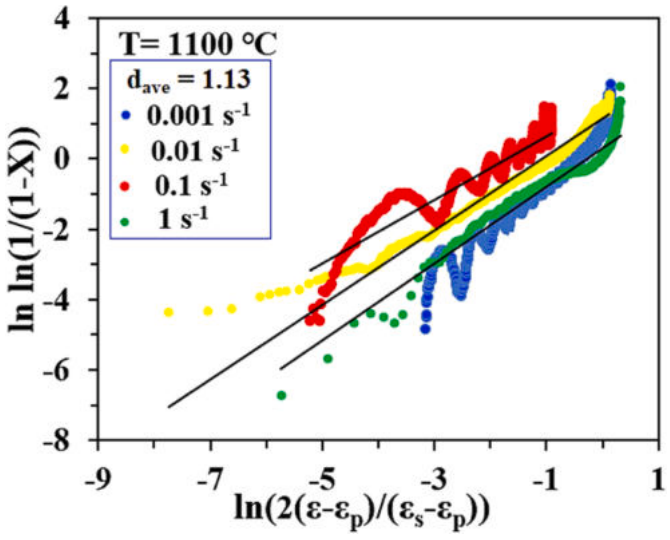

Fig. 12. Relationship between $\ln\ln(1/1\text{-}X_{DRX})$ versus $\ln(2(\varepsilon\text{-}\varepsilon_p)/(\varepsilon_s\text{-}\varepsilon_p))$ at 1100 °C and different strain rates for determination of k and d.

temperature range of 950–1050 °C for all strain rates.

For exploring the reason for lack of DRXed grains in deformed samples in the temperature range of 950–1050 °C, the $\acute{\gamma}$ precipitates evolutions before deformation and after heating and holding at deformation temperature for 5 min and then water quenching are studied (Fig. 8). As shown in Fig. 8, the microstructures contain numerous $\acute{\gamma}$ precipitates in comparison with the homogenized one in Fig. 3(d), which have been formed during the heating process. Fig. 8 confirms that coarsening and decreasing of concentration of precipitates also occur with the increase of the temperature from 950 °C to 1050 °C. The average size and volume fraction of precipitates at temperatures of 950 °C, 1000 °C and 1050 °C are estimated to be as 35 nm, 56 nm and 68 nm, and 57 %, 48 % and 34 %, respectively. Based on nucleation theory of precipitates in solid phase [31–33,45], it is expressed that with increasing the temperature, the mismatch level of $\acute{\gamma}$ precipitates in γ matrix decreases which leads to nucleation and formation of spherical coarse precipitates with low surface energy.

Rolett et al. [31] indicated that DRX is affected by precipitates distribution in alloy matrix with according to following equation:

$$D = \frac{f_v}{r} \quad \text{(Eq. 6)}$$

where f_v and r are volume fraction and radius of precipitates, respectively.

They reported that precipitates can act as an obstacle against DRX progression when D is $> 0.2\ 2\ \mu m^{-1}$ [31,45]. In this study, D values for the temperatures of 950 °C, 1000 °C and 1050 °C are calculated as 16.3 μm^{-1}, 8.57 μm^{-1} and 5 μm^{-1} which confirm the precipitates role as an obstacle against DRX development.

During hot deformation process eg. 950–1050 °C and strain rate of 0.001 s^{-1}, two phenomena of coarsening (based on agglomeration or Ostwald ripening) and shape change occur in the precipitates morphology. With the increase of the process temperature, the precipitates morphology varies from fine and spherical shape to coarse and oval shape which are accompanied with decreasing the concentration [10,47,48]. Applying the pressure during hot deformation also leads to variation of the precipitates distribution (red arrows in Fig. 9). As shown in Fig. 9, at high temperatures, the precipitates tend to connect together to form a lamellar structure as rafting, which is a well-known mechanism in Ni-based superalloys. Rafting phenomenon in Ni-based superalloys can be due to local movement of γ/ $\acute{\gamma}$ interface which its driving force is provided by the change in the elastic energy produced by the lattice mismatch. This lamellar morphology causes hard movement of dislocations during creep process [49]. Pollak et al. [50] reported the formation of the lamellar structure with preferred orientation of <100> due to the decrease of the elastic energy between precipitates and matrix [51].

3.3.2. *Microstructures in the temperature range of 1100–1200 °C*

Microstructures of deformed samples at 1100 °C, 1150 °C and 1200 °C and strain rates of 0.001 s^{-1} and 0.1 s^{-1} have been shown in Fig. 10. The presence of new fine grains near to the grain boundaries and into the initial grains confirms DRX. The plot of the average grain size of DRXed grains versus temperature and strain rate is illustrated in Fig. 11. Results show that with the increase of strain rate from 0.01 s^{-1} to 1 s^{-1}, DRXed grain size and its volume fraction are decreased. For eg., at 1150 °C and with the change of the strain rate from 0.01 to 1 s-1, the size and the volume fraction of DRXed grains are decreased from 61 μm to 91 % to 47 μm and 83 %, respectively. It has been reported that lower strain rate provides enough time for grain boundaries migration and development of DRX [26,52]. Also, with increasing the temperature from 1100 °C to 1200 °C, the size and volume fraction of DRXed grains are increased (for eg., DRXed grain size increases from 72.8 μm to 223.82 μm, respectively).

Generally, Avrami equation is used to estimate work softening and

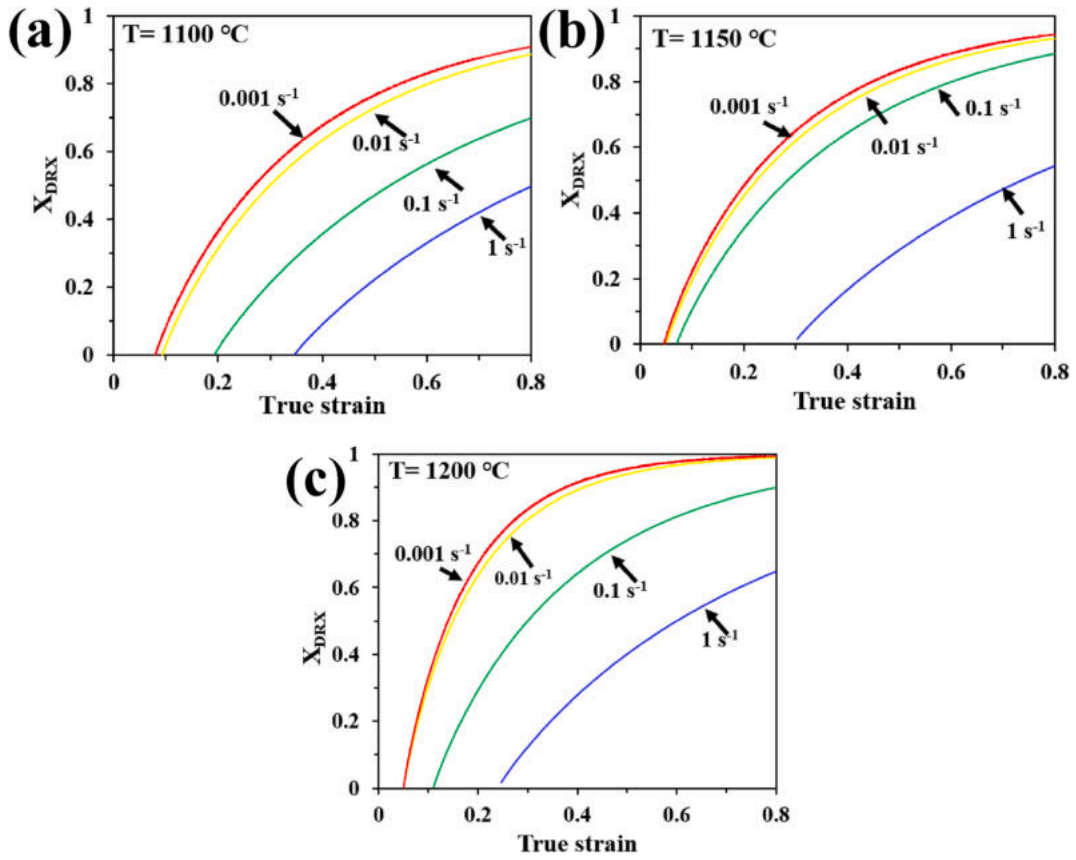

Fig. 13. Plots of X_{DRX}-strain in the strain rate range of 0.001–1 s^{-1} and temperatures of (a) 1100 °C, (b) 1150 °C and (c) 1200 °C.

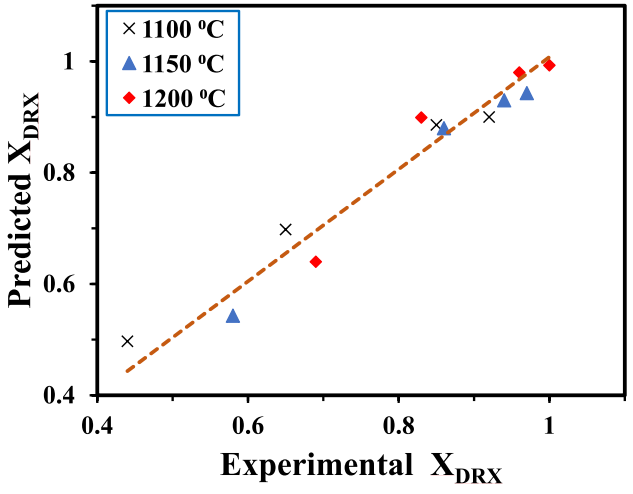

Fig. 14. The plot of predicted X_{DRX} versus experimental X_{DRX}.

volume fraction of DRXed grains by Eq. (7) [53–55]:

$$X_{DRX} = 1 - \exp\left[-k\left(\frac{2(\varepsilon - \varepsilon_p)}{(\varepsilon_p - \varepsilon_s)}\right]^d \quad \text{(Eq. 7)}$$

where ε_p and ε_s are defined as peak and steady state strains, respectively. d and k are material constants.

X_{DRX} can be also deterimend by Eq. (8):

$$X_{DRX} = \frac{\sigma_p - \sigma}{\sigma_p - \sigma_s} \quad \text{(Eq. 8)}$$

The values of σ_p, σ_s, ε_p and ε_s obtained from the true stress-true strain curves of AD730 are reported in Table 3.

With taking the logarithm from Eq. (7), the average values of k and d can be determined by drawing the ln ln(1/1-X_{DRX}) versus ln (2(ε-ε_p)/(ε_s-ε_p)) plot (Fig. 12) based on Eq. 9

$$\ln\ln\left(\frac{1}{1 - X_{DRX}}\right) = \ln k + d \ln\left(2\frac{(\varepsilon - \varepsilon_p)}{(\varepsilon_p - \varepsilon_s)}\right) \quad \text{(Eq. 9)}$$

So, the average values of k and d are reported as 0.00249 and 1.13, respectively.

With drawing X_{DRX} versus strain plots based on Eq. (7), S shape curves (Fig. 13) are obtained that designate development of DRX (nucleation and growth of new grains) during hot deformation process is affected by diffusion phenomena. Therefore, it depends on the process temperature and strain rate. X_{DRX} develops by increasing the temperature and/or decreasing the strain rate, while a full DRXed structure can be achieved at 1200 °C and 0.001 s^{-1}.

Fig. 14 shows a comparative plot between the Predicted and experimental X_{DRX} obtained at 1100 °C, 1150 °C and 1200 °C under different strain raes and strain of 0.8. Results confirm that there is a good coincidence between calculated and experimental values with regression value (R^2) of 0.997.

To study DRX mechanisms in the temperature range of 1100–1200 °C, microstructures of deformed samples at 1150 °C and 0.1 s^{-1} in different strains of 0.2, 0.4 and 0.6 have been illustrated in Fig. 15.

Microstructure at the start of the deformation process at strain of 0.2

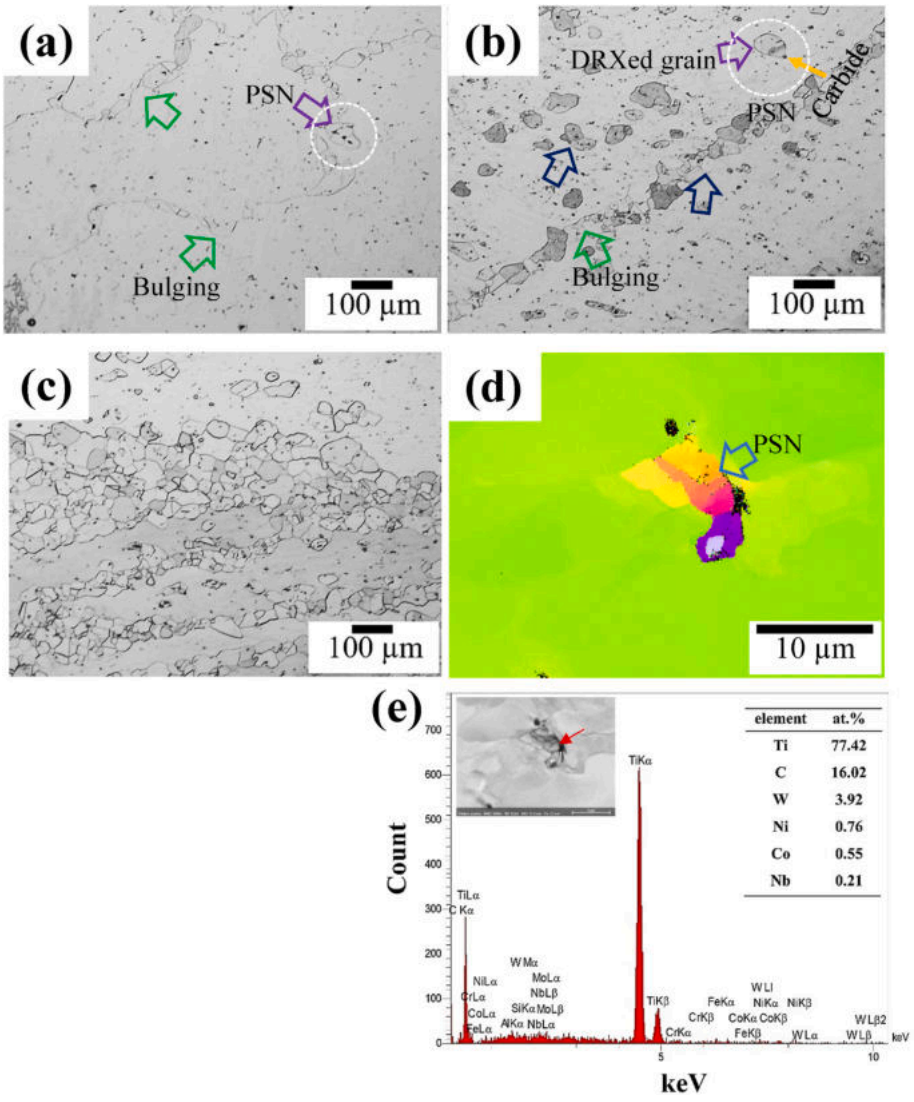

Fig. 15. Optical micrographs of deformed samples at 1150 °C-0.1 s^{-1} and strains of (a) 0.2, (b) 0.4 and (c) 0.6; (d) high magnification EBSD image showing the PSN mechanism and the formation of fine DRXed grains around the carbide particle and (e) EDX analysis of the dark area indicating of the presence of MC type carbide around the fine DRXed grains.

(Fig. 15(a)) shows that DRXed grains have been formed in the parts of serrated grain boundaries especially around the triple points. In initial strains of deformation, the deformation is affected by a high strain gradient around the grain boundaries due to non-uniform distribution of strain which leads to local migration of grain boundaries as serrations or bulging into the grains with more dislocations to decrease the system energy by nucleation of new grains. This mechanism is defined as DDRX which is introduced as a main mechanism of work softening in low strains of deformation in AD730 and occurs by plastic strain induced grain boundary migration. In this mechanism, dislocations formed during deformation are rearranged to form subgrains and then with approaching a critical size and formation of a stable nucleus develop a DRXed microstructure [18,31,56].

With further increase of the strain to 0.4 and 0.6 (Fig. 15(b and c)), the volume fraction of DRXed grains increases to form a necklace structure. Also, it is observed that some new grains have nucleated near the MC carbides by PSN mechanism (Fig. 15(d and e)). The presence of MC hard particles (~1395 HV) with size of almost 3 μm and volume fraction of 5 % in γ soft matrix (~330 HV) can provide an effective contribution in development of DRX of Ni based superalloy [30]. Semiatin et al. [57] expressed that DRX in waspaloy occurs by two mechanisms of DDRX and PSN. Sani et al. [32] have reported that during hot deformation of Co-based superalloy with initial coarse grains, PSN mechanism around the carbide particles with size of 2 μm is introduced as a main mechanism of DRX. Momeni et al. [33] investigated the effect of PSN on DRX of Incoloy 901 superalloy in the temperature range of 950–1100 °C. They indicated that the particles contribute to DRX progression by PSN when f_v/r is more than 0.2 μm^{-1}.

For more examination of DRX mechanism in this conditions, EBSD micrographs of deformed sample at 1150 °C and strain rate of 0.1 s^{-1} and strain of 0.6 with the changes of the point to point and point to origin orientations in the lines of A-B and C-D are illustrated in Fig. 16. Results show that in the long of these lines, the variations of point to origin orientation in distance of 30–35 μm are more than 10° which

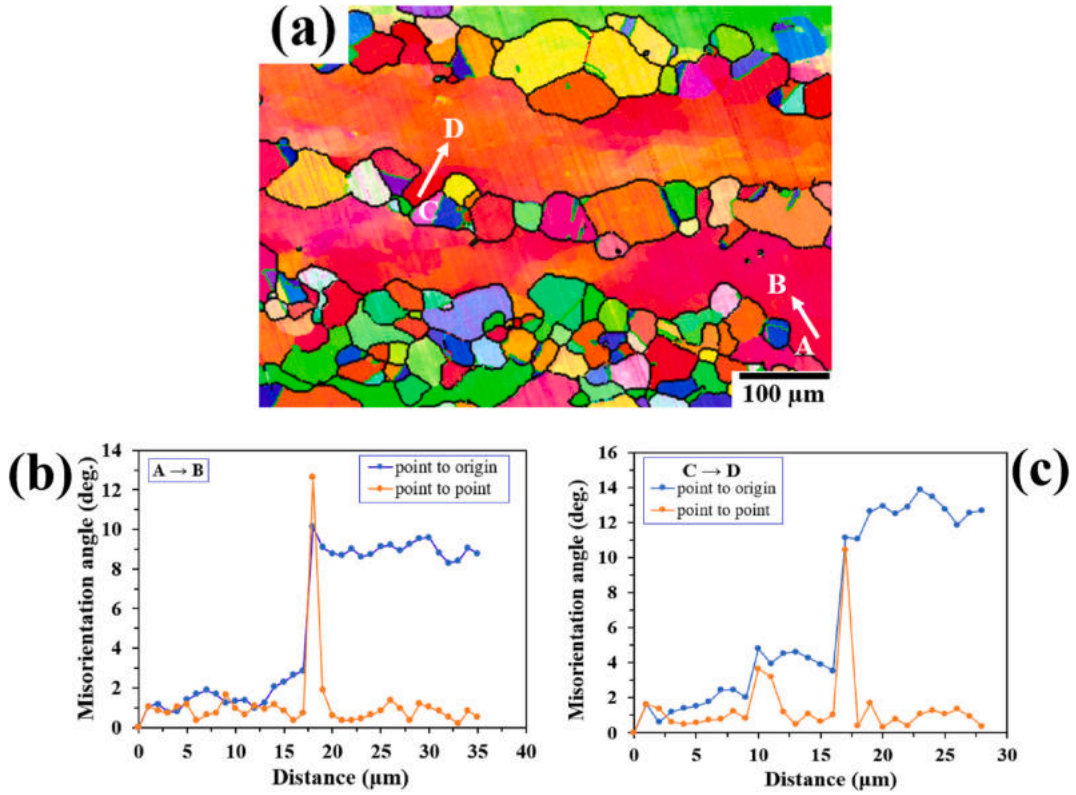

Fig. 16. (a) EBSD micrograph of deformed sample at 1150 °C and strain rate of 0.1 s^{-1} and strain of 0.6 with the changes of the point to point and point to origin orientations in the lines of (b) A-B and (c) C-D.

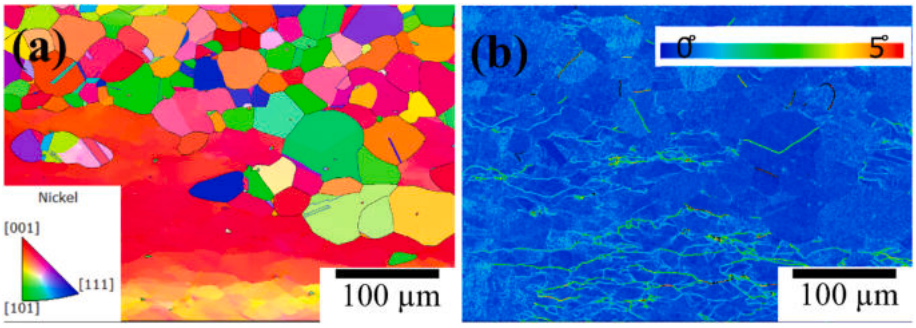

Fig. 17. EBSD micrographs of deformed sample at 1150 °C and strain rate of 0.1 s^{-1} and strain of 0.6; (a) IPF and (b) KAM maps.

designate with the increase of strain to 0.6, medium and high angle boundaries form close to initial grain boundaries. It confirms that for development of a DRXed structure with the increase of strain, first, dislocations rearrangement occurs with formation subgrains to form a low energy structure, and then these subgrains grow while consume the dislocations to reach a critical size to form a stable nucleus.

The EBSD inverse pole figure (IPF) map in Fig. 17(a) indicates the presence of equiaxed grains with random orientation at elevated temperatures due to DRX. The kernel average misorientation (KAM) map presented in Fig. 17(b) at 1150 °C, 0.1 s^{-1} and strain of 0.6 asserts high dislocation density and low angle boundaries in the initial deformed grains as compared to DRXed grains. High dislocation density in initial deformed grains in the start of the process (work hardening step) increases local misorientation which leads to the formation of subgrains and finally DRXed grains in deformed regions with continuation of deformation [58].

Fig. 18(a) presents a grain boundary map (GBM) of deformed sample at 1150 °C, 0.1 s^{-1} and strain of 0.6. HAGBs ($\theta > 15°$) with black color and twin boundaries including Σ3 (60°/<111>), Σ9 (38.94°/<110>) and Σ27 (31.58°/<110>) [24,59,60] are observed with colors of blue, green and brown, respectively. The existence of twin boundaries in DRXed grains indicates the formation of twins in the growth step of these grains. Also, high fraction of blue boundaries indicates that more twins are $\sum 3$ type. Some researchers stated that with the increase of serrated grain boundaries during DRX, twins can develop nucleation and growth of DRXed grains in Ni-based superalloys [27,59]. The development of twin boundaries during hot deformation of Ni-based superalloys can be investigated by two issues: (i) the decrease of initial twins effect with the increase of strain by their transformation to HAGBs as a result of the change of initial grains orientation [59] which is in agreement with Ebrahimi et al. findings [58]; (ii) nucleation and growth of new twins in the DRXed grains [27]. In present work, with considering the initial coarse grains of AD730 before deformation, twin boundaries have a minor role in the start of DRX. So, AD730 similar to other Ni-based superalloys with low SFE tend to form annealing twins during DRX by the random growth mechanism. These twins are formed by interaction

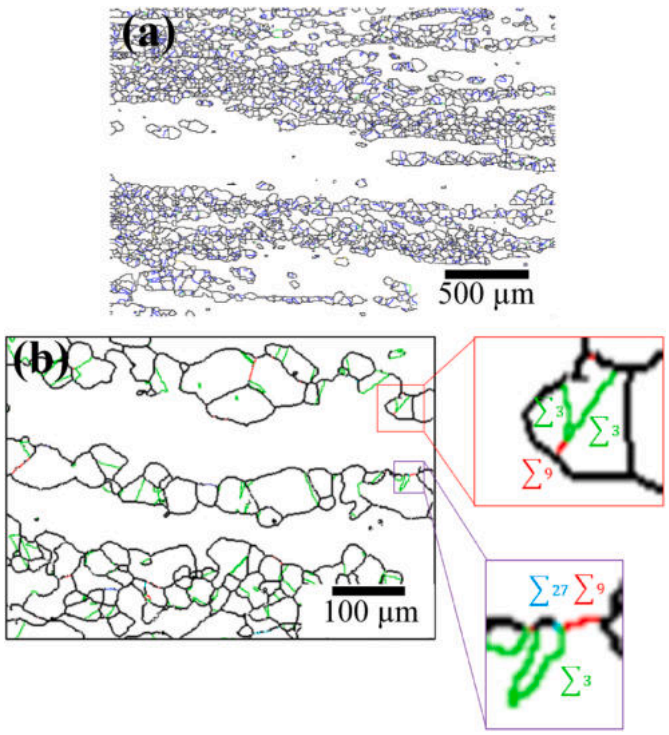

Fig. 18. (a) A grain boundaries map (GBM) of deformed sample at 1150 °C, 0.1 s^{-1} and strain of 0.6 (HAGBs (θ > 15°) with black color and twin boundaries including Σ3, Σ9 and Σ27 with colors of green, red and blue have been characterized) and (b) showing the interaction of twins (Σ3: green, Σ9: red, Σ27: blue).

between HAGBs and the SFE region [27]. The formation rate of twins can increase with fast movement of boundaries at elevated temperatures [59]. The formation of twins in DRXed grains leads to the decrease of grain boundaries energy and enhanement of their mobility. So, the presence of twins improves growth of DRXed grains. It has been reported that twins accelerate dislocations absorption and separate the bulging regions from initial grains [61–63].

During hot deformation, twins can interact together to form Σ3 and $\Sigma3^n$ (n > 1) ones [60,61]. For eg., the interaction of initial Σ3 twins leads to formation of Σ9 twin boundaries in accordance with Σ3 + Σ3 relationship (Fig. 18(b)). With formation of Σ9 boundary, it can interact with Σ3 boundary to form Σ3 and Σ27 twin boundaries with relationships of Σ3 + Σ9 → Σ27 and Σ3 + Σ9 → Σ3 [26,64,65]. These interactions can sometimes occur in AD730 similar to other Ni-based superalloys [66]. The presence of twin boundaries with low fault energy and vacancy can increase corrosion resistance and fatigue strength [67,68].

For better understanding, a schematic illustration of DRX mechanisms in AD730 is shown in Fig. 19. Based on the presented model in Fig. 19, AD730 consists of coarse grains, low angle boundaries and carbides at the initial stage of the deformation (Fig. 19(b)). With the increase of the strain and work hardening stage, dislocation density rises rapidly around the grain boundaries and carbide particles which results in the increase of the internal energy (Fig. 19(c)). With continuation of the deformation and after the critical strain, work softening stage strats with the formation of fine DRXed grains around bulged grain boundaries (DDRX mechanism) and carbide particles (PSN mechanism) which decreases the internal energy (Fig. 19(d)). In this stage, twins present a positive effect and develop DRX with formation of new orientations in DRXed grains. In the steady state stage, a balance between work hardening and work softening occurs which is accompanied with grain refining (Fig. 19(e)).

4. Conclusions

In this study, hot deformation behavior and microstructural evaluation of AD730 Ni-based superalloy were investigated in a wide temperature range of 950–1200 °C and strain rates of 0.001 s–1 to 1 s-1 up to the strain of 0.8. Following points were extracted.

1) Flow behavior and microstructure changes of AD730 during hot deformation process were dependent on the solution temperature of $\acute{\gamma}$ precipitates at 1079 °C, which were divided to two temperature ranges of 950–1050 °C and 1100–1200 °C.
2) In the temperature range of 950–1050 °C, the presence of fine $\acute{\gamma}$ precipitates caused high stress levels, high activation energy of 1160.45 kJ/mol and nonuniform deformation due to their role as an obstacle against work softening and DRX development.

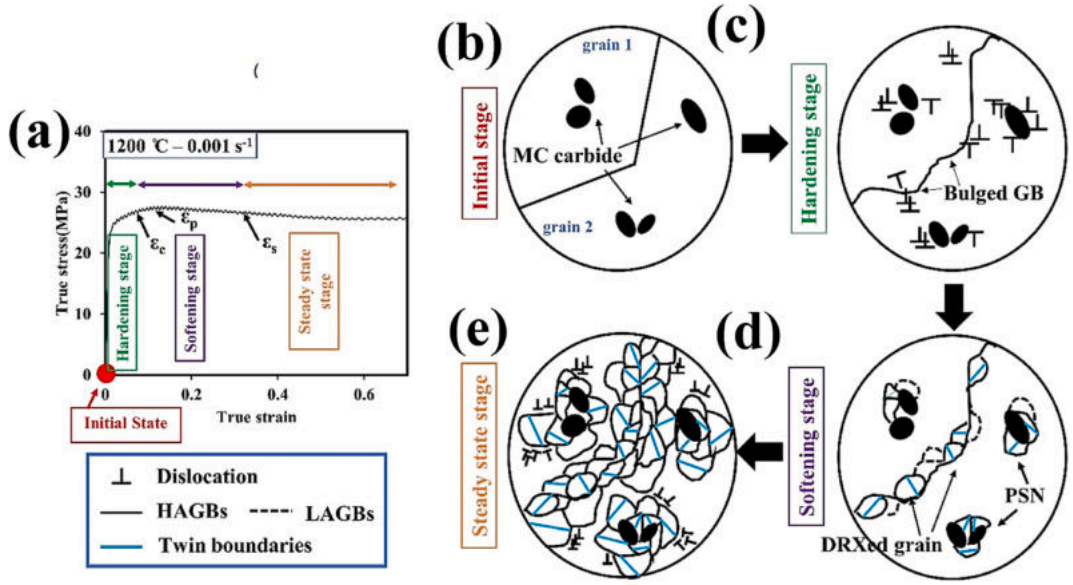

Fig. 19. A schematic illustration of microstructure development of AD730 during hot deformation at 1200 °C and 0.001 s^{-1}; (a) the true stress-true strain curve, microstructures in (b) initial stage, (c) work hardening stage, (d) work softening stage and (e) steady state stage.

3) In the temperature range of 1100–1200 °C, the dissolution of fine precipitates decreased considerably stress levels and activation energy to 468.32 kJ/mol which was corresponded to easier occurrence of DRX.
4) In the temperature range of 1100–1200 °C, DRXed structure by DDRX and PSN mechanisms was developed by the formation of the twins. Also, the volume fraction of DRXed grains increased with increasing the temperature and decreasing the strain rate.

Declaration of competing interest

The authors declare that they have no known competing financial interests or personal relationships that could have appeared to influence the work reported in this paper.

References

[1] Devaux A, Picqué B, Gervais MF, Georges E, Poulain T, Héritier P. AD730™ - a new nickel-based superalloy for high temperature engine rotative parts. Superalloys. John Wiley & Sons, Inc.; 2012. p. 911–9.
[2] Devaux A, Georges E, Héritier P. Development o f new C&W superalloys for high temperature disk applications. Adv Mater Res 2011;278:405–10.
[3] Devaux A, Georges E, Héritier P. Properties of new C&W superalloys for high temperature disk applications. Superalloy 718 and derivatives. John Wiley & Sons, Inc; 2010. p. 222–35.
[4] Devaux A, Berglin L, Thebaud L, Delattre R, Crozet C, Nodin O. Mechanical properties and development of supersolvus heat treated new nickel base superalloy AD730TM. MATEC Web of Conferences 2014;14:01004.
[5] Thébaud L, Villechaise P, Crozet C, Devaux A, Béchet D, Franchet J-M, Rouffié A-L, Mills M, Cormier J. Is there an optimal grain size for creep resistance in Ni-based disk superalloys? Materials Science and Engineering: A 2018;716:274–83.
[6] Tabaie S, Rézaï-Aria F, Flipo BC, Jahazi M. Grain size and misorientation evolution in linear friction welding of additively manufactured IN718 to forged superalloy AD730. Mater Char 2021;171:110766.
[7] Masoumi F, Shahriari D, Monajati H, Cormier J, Flipo BCD, Devaux A, Jahazi M. Linear friction welding of AD730™ Ni-base superalloy: process-microstructure-property interactions. Mater Des 2019;183:108117.
[8] Masoumi F, Jahazi M, Cormier J, Shahriari D. Dissolution kinetics and morphological changes of γ′ in AD730TM superalloy. MATEC Web of Conferences, EDP Sciences; 2014, 13005.
[9] Devaux A, Helstroffer A, Cormier J, Villechaise P, Douin J, Hantcherli M, Pettinari-Sturmel F. Effect of aging heat-treatment on mechanical properties of AD730™ superalloy. 8th international symposium on superalloy 718 and derivatives. Hoboken, NJ, USA: John Wiley & Sons, Inc.; 2014. p. 521–35.
[10] Mrozowski N, Hénaff G, Hamon F, Rouffié A-L, Franchet J-M, Cormier J, Villechaise P. Aging of γ′ precipitates at 750 °c in the nickel-based superalloy ad730tm: a thermally or thermo-mechanically controlled process? Metals 2020;10:426.
[11] Pettinari-Sturmel F, Hantcherli M, Vultos W, Marcelot C, Tisseyre M, Cours R, Douin J, Villechaise P, Cormier J. Contribution of primary γ′ precipitates in the deformation creep mechanisms in the ni-based polycrystalline ad730 tm superalloy, Superalloys 2020. Proceedings of the 14th international symposium on superalloys. Springer; 2020. p. 613–8.
[12] Zhou Q, An T, Zhang K, Zhou C, Qian H, Ying D, Li Y, Zhang L. Effect of microstructure on hot corrosion behavior of new superalloy Ad 730 in 75 wt% Na2SO4+ 25 wt% NaCl molten salt. Mater Lett 2023;341:134231.
[13] Zhou Q, Zhang K, Zhou C, Qian H, Ying D, Li Y, Li L, Zhang L. Comparative hot corrosion behavior of new nickel-based superalloy ad 730 and inconel 718 in 75 wt.% Na2SO4+ 25 wt.% NaCl molten salt medium at 700° C. J Mater Eng Perform 2025;34(3):2585–99.
[14] Konkova T, Rahimi S, Mironov S, Baker T. Effect of strain level on the evolution of microstructure in a recently developed AD730 nickel based superalloy during hot forging. Mater Char 2018;139:437–45.
[15] Coyne-Grell A, Blaizot J, Rahimi S, Violatos I, Nouveau S, Dumont C, Nicolaÿ A, Bozzolo N. Evolution of γ′ precipitation during the early stages of industrial forging of a nickel-based superalloy. Metall Mater Trans 2023;54(5):2022–36.
[16] Blaizot J, Finet L, Chabrier A, Fornara A, Fage M, Remichi R, Dadé M, Perez M. Gamma prime precipitation in cast and wrought AD730® superalloy. International symposium on superalloys. Springer; 2024. p. 762–73.
[17] Coyne-Grell A, Pérez M, Violatos I, Blaizot J, Dumont C, Nouveau S. Precipitation of γ′ in two γ-γ′ ni-based superalloys during the solvus transition stage of ingot to billet conversion: Effects on γ grain structure and implications for open die forging. International symposium on superalloys. Springer; 2024. p. 727–40.
[18] Huang K, Logé R. A review of dynamic recrystallization phenomena in metallic materials. Mater Des 2016;111:548–74.
[19] Chen X-M, Lin Y, Wen D-X, Zhang J-L, He M. Dynamic recrystallization behavior of a typical nickel-based superalloy during hot deformation. Mater Des 2014;57:568–77.
[20] Wang Y, Shao WZ, Zhen L, Zhang XM. Microstructure evolution during dynamic recrystallization of hot deformed superalloy 718. Materials Science and Engineering: A 2008;486(1–2):321–32.
[21] Chen X-M, Lin YC, Chen M-S, Li H-B, Wen D-X, Zhang J-L, He M. Microstructural evolution of a nickel-based superalloy during hot deformation. Mater Des 2015;77:41–9.
[22] Lin Y-C, Deng J, Jiang Y-Q, Wen D-X, Liu G. Hot tensile deformation behaviors and fracture characteristics of a typical Ni-based superalloy. Mater Des 2014;55:949–57.
[23] Liu F, Chen J, Dong J, Zhang M, Yao Z. The hot deformation behaviors of coarse, fine and mixed grain for Udimet 720Li superalloy. Materials Science and Engineering: A 2016;651:102–15.
[24] Zhong X, Huang L, Liu F. Discontinuous dynamic recrystallization mechanism and twinning evolution during hot deformation of Incoloy 825. J Mater Eng Perform 2020;29:6155. 5169.
[25] Zhang Y, Tao N, Lu K. Effects of stacking fault energy, strain rate and temperature on microstructure and strength of nanostructured Cu–Al alloys subjected to plastic deformation. Acta Mater 2011;59(15):6048–58.
[26] Wang M, Sun C, Fu M, Liu Z, Qian L. Study on the dynamic recrystallization mechanisms of Inconel 740 superalloy during hot deformation. J Alloys Compd 2020;820:153325.
[27] Azarbarmas M, Aghaie-Khafri M, Cabrera J, Calvo J. Dynamic recrystallization mechanisms and twining evolution during hot deformation of Inconel 718. Materials Science and Engineering: A 2016;678:137–52.
[28] Zeng X, Huang L, Liu W, Luo J, Pei L, Song W, Mi Z, Xu X. Hot deformation behavior and dynamic recrystallization mechanism of GH2132 superalloy. J Alloys Compd 2024;1009:176798.
[29] Song X, Tang Z, He X, Jia L, Li G, He J, Wang X. Hot deformation behavior and microstructure evolution of a novel as-forged Ni-based superalloy. J Alloys Compd 2025;1024:180195.
[30] Huang K, Marthinsen K, Zhao Q, Logé RE. The double-edge effect of second-phase particles on the recrystallization behaviour and associated mechanical properties of metallic materials. Prog Mater Sci 2018;92:284–359.
[31] Rollett A, Humphreys F, Rohrer GS, Hatherly M. Recrystallization and related annealing phenomena. Elsevier; 2004.
[32] Sani SA, Arabi H, Ebrahimi GR. Hot deformation behavior and DRX mechanism in a γ-γ′/cobalt-based superalloy. Mater Sci Eng; A 2019;764:138165.
[33] Momeni A, Abbasi S, Morakabati M, Badri H, Wang X. Dynamic recrystallization behavior and constitutive analysis of Incoloy 901 under hot working condition. Mater Sci Eng; A 2014;615:51–60.
[34] Wang Y, Zhen L, Shao W, Yang L, Zhang X. Hot working characteristics and dynamic recrystallization of delta-processed superalloy 718. J Alloys Compd 2009;474(1–2):341–6.
[35] Beladi H, Cizek P, Hodgson PD. Dynamic recrystallization of austenite in Ni-30 Pct Fe model alloy: microstructure and texture evolution. Metall Mater Trans 2009;40:1175–89.
[36] Choi BG, Kim IS, Kim DH, Jo CY. Temperature dependence of MC decomposition behavior in Ni-base superalloy GTD 111. Materials Science and Engineering: A 2008;478(1–2):329–35.
[37] Chamanfar A, Jahazi M, Gholipour J, Wanjara P, Yue S. Evolution of flow stress and microstructure during isothermal compression of Waspaloy. Materials Science and Engineering: A 2014;615:497–510.
[38] Jahangiri M, Arabi H, Boutorabi S. High-temperature compression behavior of cast and homogenized IN939 superalloy. Metall Mater Trans 2013;44:1827–41.
[39] Wan Z, Hu L, Sun Y, Wang T, Li Z. Hot deformation behavior and processing workability of a Ni-based alloy. J Alloys Compd 2018;769:367–75.
[40] Li H, Zhuang X, Lu S, Antonov S, Li L, Feng Q. Hot deformation behavior and flow stress modeling of a novel CoNi-based wrought superalloy. J Alloys Compd 2022;894:162489.
[41] Zhang M, Zhang B, Jiao X, Ding H. Hot deformation behaviors and microstructure evolution of a supersaturated nickel-based superalloy. Mater Char 2024;211:113915.
[42] Ershadikia H, Ebrahimi G, Ezatpour H, Momeni A. Correction to: effect of boron on the microstructure evolution and dynamic recrystallization kinetics of ALLVAC718Plus superalloy. J Mater Eng Perform 2021;30(1):228. 228.
[43] Sun C, Liu G, Zhang Q, Li R, Wang L. Determination of hot deformation behavior and processing maps of IN 028 alloy using isothermal hot compression test. Materials Science and Engineering: A 2014;595:92–8.
[44] Wu H-Y, Zhu F-J, Wang S-C, Wang W-R, Wang C-C, Chiu C-H. Hot deformation characteristics and strain-dependent constitutive analysis of Inconel 600 superalloy. J Mater Sci 2012;47:3971–81.
[45] Monajati H, Taheri A, Jahazi M, Yue S. Deformation characteristics of isothermally forged UDIMET 720 nickel-base superalloy. Metall Mater Trans 2005;36(4):895–905.
[46] Sajjadi SA, Chaichi A, Ezatpour HR, Maghsoudlou A, Kalaie MA. Hot deformation processing map and microstructural evaluation of the Ni-based superalloy IN-738LC. J Mater Eng Perform 2016;25:1269–75.
[47] Wu Y, Li C, Xia X, Liang H, Qi Q, Liu Y. Precipitate coarsening and its effects on the hot deformation behavior of the recently developed γ'-strengthened superalloys. J Mater Sci Technol 2021;67:95–104.
[48] Ge L, Zhang XN, Guo WG, Dong P, Yu T, Liu CP, Yuan Y, Wang CY, Zhang Z. The coarsening behavior of γ′ phases in Ni-Al binary model single crystal superalloy at 1000 °C. J Alloys Compd 2022;911:164989.
[49] Baldan A. Review Progress in Ostwald ripening theories and their applications to the γ′-precipitates in nickel-base superalloys Part II Nickel-base superalloys. J Mater Sci 2002;37:2379–405.
[50] Pollock TM, Argon A. Directional coarsening in nickel-base single crystals with high volume fractions of coherent precipitates. Acta Metall Mater 1994;42(6):1859–74.

[51] Maebashi T, Doi M. Coarsening behaviours of coherent γ′ and γ precipitates in elastically constrained Ni–Al–Ti alloys. Materials Science and Engineering: A 2004;373(1–2):72–9.
[52] Zhang H, Zhang K, Zhou H, Lu Z, Zhao C, Yang X. Effect of strain rate on microstructure evolution of a nickel-based superalloy during hot deformation. Mater Des 2015;80:51–62.
[53] Mirzaee M, Keshmiri H, Ebrahimi GR, Momeni A. Dynamic recrystallization and precipitation in low carbon low alloy steel 26NiCrMoV 14-5. Materials Science and Engineering: A 2012;551:25–31.
[54] Sani SA, Ebrahimi G, Rashid AK. Hot deformation behavior and dynamic recrystallization kinetics of AZ61 and AZ61+ Sr magnesium alloys. J Magnesium Alloys 2016;4(2):104–14.
[55] Ezatpour HR, Torabi-Parizi M, Ebrahimi GR, Momeni A. Effect of micro-alloy elements on dynamic recrystallization behavior of a high-manganese steel. Steel Res Int 2018;89(7):1700559.
[56] Sakai T, Belyakov A, Kaibyshev R, Miura H, Jonas JJ. Dynamic and post-dynamic recrystallization under hot, cold and severe plastic deformation conditions. Prog Mater Sci 2014;60:130–207.
[57] Semiatin S, Weaver D, Kramb R, Fagin P, Glavicic M, Goetz R, Frey N, Antony M. Deformation and recrystallization behavior during hot working of a coarse-grain, nickel-base superalloy ingot material. Metall Mater Trans 2004;35:679–93.
[58] Ebrahimi G, Momeni A, Ezatpour H, Jahazi M, Bocher P. Dynamic recrystallization in Monel400 Ni-Cu alloy: mechanism and role of twinning. Materials Science and Engineering: A 2019;744:376–85.
[59] Zhang H, Zhou H, Qin S, Liu J, Xu X. Effect of deformation parameters on twinning evolution during hot deformation in a typical nickel-based superalloy. Materials Science and Engineering: A 2017;696:290–8.
[60] Prithiv T, Bhuyan P, Pradhan S, Sarma VS, Mandal S. A critical evaluation on efficacy of recrystallization vs. strain induced boundary migration in achieving grain boundary engineered microstructure in a Ni-base superalloy. Acta Mater 2018;146:187–201.
[61] Randle V. Twinning-related grain boundary engineering. Acta Mater 2004;52(14):4067–81.
[62] Wang Y, Shao WZ, Zhen L, Yang L, Zhang XM. Flow behavior and microstructures of superalloy 718 during high temperature deformation. Materials Science and Engineering: A 2008;497(1–2):479–86.
[63] Momeni A, Ebrahimi G, Jahazi M, Ezatpour H. Microstructure characterization and dynamic recrystallization behavior of Ni–Cu alloy during hot deformation. Mech Mater 2024;193:105002.
[64] Yang J, Luo J, Li X, Li M. Evolution mechanisms of recrystallized grains and twins during isothermal compression and subsequent solution treatment of GH4586 superalloy. J Alloys Compd 2021;850:156732.
[65] Wang W, Brisset F, Helbert A, Solas D, Drouelle I, Mathon M, Baudin T. Influence of stored energy on twin formation during primary recrystallization. Materials Science and Engineering: A 2014;589:112–8.
[66] Jiang H, Dong J, Zhang M, Yao Z. Evolution of twins and substructures during low strain rate hot deformation and contribution to dynamic recrystallization in alloy 617B. Materials Science and Engineering: A 2016;649:369–81.
[67] Quan G-z, Zhang Y-q, Zhang P, Ma Y-y, Wang W-y. Correspondence between low-energy twin boundary density and thermal-plastic deformation parameters in nickel-based superalloy. Trans Nonferrous Metals Soc China 2021;31(2):438–55.
[68] Detrois M, Goetz RL, Helmink RC, Tin S. Modeling the effect of thermal–mechanical processing parameters on the density and length fraction of twin boundaries in Ni-base superalloy RR1000. Materials Science and Engineering: A 2015;647:157–62.